2022 26th International Conference on Pattern Recognition (ICPR)
August 21-25, 2022, Montréal, Québec, Canada

Hand Crafted Features for Efficient Lung Cancer Diagnosis Using Stacked Autoencoder

Ahmed Shaffie[1], Ahmed Soliman[1], Victor van Berkel[2], and Ayman El-Baz[1]

[1]BioImaging Laboratory, Bioengineering Department, University of Louisville, Louisville, KY, USA.
[2]Department of Cardiovascular and Thoracic Surgery, University of Louisville, Louisville, KY, USA.

2022 26th International Conference on Pattern Recognition (ICPR) | 978-1-6654-9062-7/22/$31.00 ©2022 IEEE | DOI: 10.1109/ICPR56361.2022.9956340

***Abstract*—The most critical steps to improve the clinical management of the lung cancer are the early detection and the accurate diagnosis. In this study, an automated system for lung cancer diagnosis from one computed tomography (CT) scan is developed to distinguish between malignant and benign nodules. This system utilizes two different kinds of features to describe the lung nodules. These features indicate the nodule's preceding growth rate, which is considered the major point in pulmonary nodule diagnosis. Analytical Local Binary Pattern is implemented to characterize the pulmonary nodule texture. Special functions called spherical harmonics are used to characterize the nodule surface. Finally, a stacked autoencoder is utilized to reduce the dimensionality of the modeled features values and to eliminate the noise in the data followed by a probability-based linear classifier to diagnose the nodule. The proposed system is tested using Lung Image Database Consortium (LIDC) database. The effectiveness of the presented framework is confirmed where the system accuracy, sensitivity, specificity, and area under the ROC curve of 93.79%, 94.36%, 92.80%, and 0.9764 respectively are achieved.**

***Index Terms*—Lung Cancer, Analytical Local Binary Pattern, Deep learning, CT Image, special functions, Medical Image Processing.**

I. Introduction

Lung cancer is by far the leading cause of death in the US and all over the world in general. This is related to the fact that it is usually diagnosed at late stages [1]. Since mortality rates are increasing intensively, it is essential to turn toward improving ways that help to early diagnose lung cancer. Computer Tomography (CT) imaging is widely used in screening lung cancer that helps to decrease the mortality rate by 20% [2]. However, lung cancer detection and diagnosis is still challenging, knowing that it is time-consuming and labor-intensive for radiologists that have to go over a large amount of CT images to give their diagnosis. As a result, for the past few decades many researchers turned toward developing multiple systems to help radiologists in the diagnosis process, not only for lung cancer but also for different kinds of cancer [3]–[8]. They used for that machine learning, deep learning, and image processing techniques [9]–[13].

Lin et al. [14] proposed a 2D convolutional neural network with Taguchi parametric optimization for lung cancer classification. They improved their results by using the Taguchi parametric eight control factors and 36 experiments of mixed levels to find out the best parameters that fits the classification task. Their results improved when using the Taguchi parameter optimization comparing to the original 2D CNN only without optimization parameters on the LIDC dataset and on other dataset from the International Society for Optics and Photonics with the support of the American Association of Physicists in Medicine (SPIE-AAPM). The false positive rate in their experiment was 0.06. kalaivani et al. [15] developed a classification framework for lung nodules based on DenseNet and adaptive boosting algorithms. They tested their algorithm on 201 lung images where 85% of them were used for training and 15% for testing. Their method achieved an accuracy of 90.85%. Ren et al. [16] developed a manifold regularized classification deep neural network (MRC-DNN) for the lung nodules classification task. They achieved an accuracy of 90%, a sensitivity of 81% and a specificity of 95%. Suresh et al. [17] proposed multiple CNNs architectures for the classification task. They generated additional images with similar characteristics as pulmonary nodules to augment their data by generative adversarial networks (GANs). They tested their algorithm on the LIDC dataset and achieved a good accuracy measures. They achieved an accuracy of 93.9%, a sensitivity of 93.4%, a specificity of 93% and an AUC of 0.93. Jiang et al. [18] developed an ensemble of 3D Dual Path Networks. In a first step they improved the representativeness of deep features by modeling the contextual correlations among adjacent locations when dividing the contextual attention. In a second step, they used a spatial attention mechanism to find the important regions for the nodules classifications. Finally, they improved the prediction efficiency by using several models. They tested their algorithm on the LIDC dataset and acheived accuracy of 90.24%. Shrey et al. [19] introduced a cascaded architecture that segments and classifies lung nodules into benign or malignant. They introduced a segmentation network where they trained their model on a public dataset to identify images that include nodules using transfer learning then classify them. Their system achieved an AUC of 95.67% and an accuracy of 97.96%. Patel et al. [20] used k-means and EK-means clustering methods on lung images. They extracted GLCM and geometrical features and classified them using artificial neural networks (ANN) and support vector machine (SVM). They achieved an accuracy of 78.50% and 87.50 for the ANN and SVM respectively. Safta et al. [9] combined MI-SVM that belong to the Multiple Instance Learning paradigms with GLCM and LBP features for the lung nodules diagnosis task. They tested their algorithm on a collection from the LIDC

dataset. They achieved an accuracy of 91.11%, a sensitivity of 69.79%, a specificity of 98.55% and an AUC of 0.9696.

All previously described CADx systems have the following gaps: *(i)* Some systems don't take into account the morphological features and feed only the raw data to a neural networks. Although the neural networks could generate their own rules to classify the nodule from the original scan, the lack of transparency on how these rules are generated is seen as an issue and makes the system appear as a black boxes that is very difficult to be interpreted. *(ii)* Some systems use only the basic shape features and are sensitive to the segmentation process which make them inaccurate. *(iii)* Some systems oversight the spatial interaction between pixels because they utilize only the Hounsefield Unit (HU) values as an appearance feature. In order to keep away from these gaps, texture and shape features are combined together in our framework. A multi-view analytical local binary pattern is developed to utilize the 3D interrelationship between the nodule voxels. The reconstruction error of a special function called spherical harmonics is used to describe the pulmonary nodules' surface intricacy and shape characteristics. Eventually, the dimensionality is reduced using a stacked autoencoder consisted of three layers followed by a probability-based linear classifier to give the final diagnoses of the nodule.

II. Methods

The proposed noninvasive lung cancer detection framework combines texture and shape characteristics of the pulmonary nodule to distinguish between malignant and benign nodules. All these characteristics are drawn out from a one-time computed tomography scan. Figure 1 illustrates the general idea of the proposed framework and all its details are listed in the following sections.

A. Multi-View Analytical Local Binary Pattern (ALBP)

Cancerous pulmonary nodules grow rapidly compared to benign ones, which make their texture irregular. These texture differences lead to a distinction in the Hounsfield unit values and will be used to distinguish between the malignant and benign nodules. A Multi-view ALBP descriptor is developed to accurately model the nodule texture and to add the spatial datum of the voxel's neighbors. This descriptor is an improvement from the traditional LBP to reduces the noise effect on the CT scans and to give a precise model for the nodule texture. This section will start with a brief description of the traditional LBP followed by a presentation for our proposed Multi-view ALBP.

1) The Traditional Local Binary Pattern (LBP): LBP is a well-recognized feature for texture classification, and was introduced by Ojala [21], [22]. In the traditional LBP, the local neighborhood around each pixel is thresholded at the central pixel value and the output binary string is considered as a binary number that is weighted as follows:

$$LBP_{N,R} = \sum_{i=1}^{N} 2^{i-1} * f(g_i - c) \tag{1}$$

where c denote the gray level of the central pixel, g_i denote the gray level of N neighbors that are evenly distributed on a circle of radius R around the central pixel, and finally

$$f(x) = \begin{cases} 1 & \text{if } x \geq 0 \\ 0 & otherwise \end{cases} \tag{2}$$

Assuming that the central pixel coordinate is the origin $(0, 0)$, then the coordinates of its N neighbors on a circle of radius R can be calculated using equation 3.

$$(x_i, y_i) = (-Rsin(2\pi i/N), Rcos(2\pi i/N)) \tag{3}$$

In the case that the coordinates are not located into the grid perfectly to get the gray level, it will be estimated by resampling using bilinear interpolation. The LBP could be applied on the three dimensions by considering all the neighbors on a sphere of radius R, which will lead to a mass of calculations and huge running time without an effective accuracy enhancement. The information inherited in the 3D volume could be utilized by extracting various group of 2D cross-sections for the 3D volume in fixed planes. Sometimes, undesirable noise or deformation happens to the CT scans because of different reasons, such as the number of photons used in the examination, the slice thickness, and the patient size. Using a hard threshold in the traditional LBP makes it very sensitive and not robust to the noise, which makes it not suitable for the nodule diagnosis application. Here are some problems that may happen when the traditional LBP is used:

(i) when the nodule has a uniform texture (like in the case of benign nodules), all the neighbor pixels should have the same label either 1 or 0. However, if a tiny noise is added to the scan (while using a hard threshold), the descriptor will label some pixels 1 and some pixels 0 depending on the noise location.

(ii) When all the neighbor pixels are greater than the pixel in the center, the traditional LBP will label all of them 1 without differentiating between the pixels that have a large difference and small one. In a similar way, when all the neighbor pixels are less than the pixel in the center, the traditional LBP will label all of them 0 without differentiating between the pixels that have large difference and small one.

2) Analytical Local Binary Pattern: In order to overcome the mentioned problems, instead of comparing the central pixel to the surrounding neighbors, we started to compute some information about the distribution of the surrounding pixels' gray levels and compare it to the average of these information, such as: mean, standard deviation, median, maximum, and minimum. The calculations for the feature vector could be divided into the following phases.

(i) Surrounding pixel resampling

To get more information about the surrounding pixels, different levels of neighborhood are involved using different values for the radius R. For each level R, there is a vector G_R that contains all the central pixel neighbors that are evenly distributed on the circle with the specified radius. When the

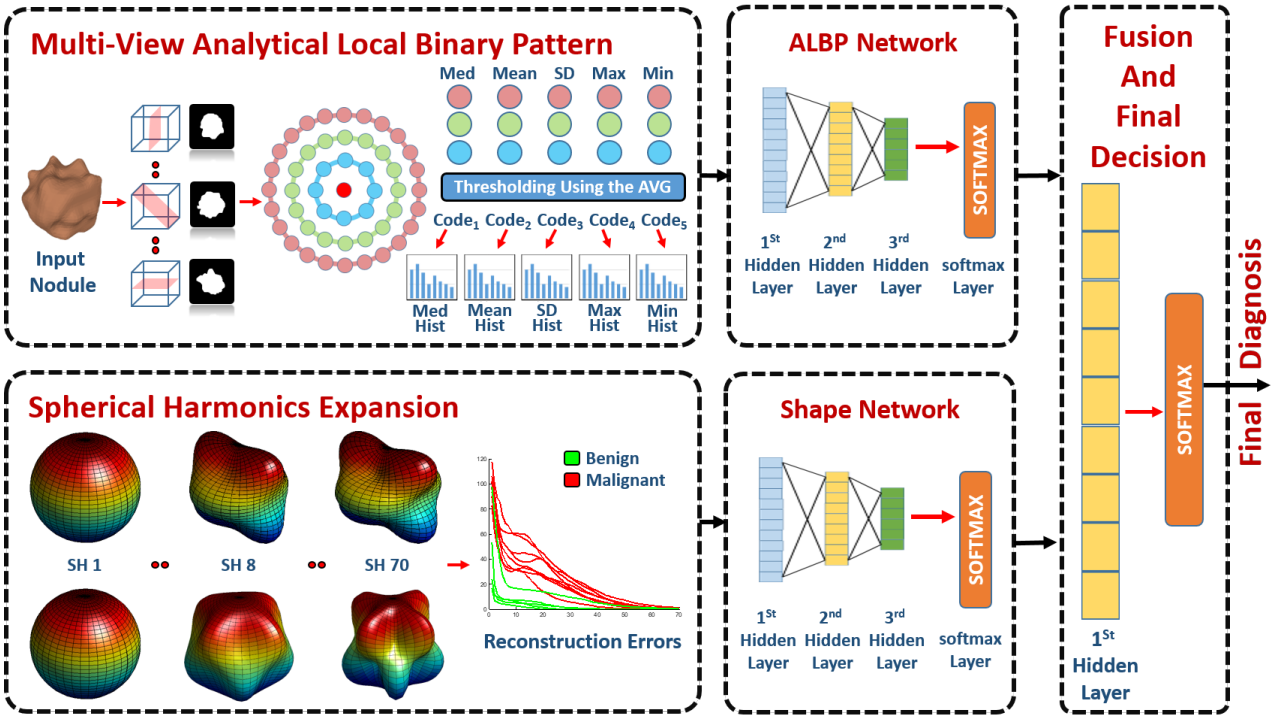

Fig. 1. Our framework for pulmonary nodules classification

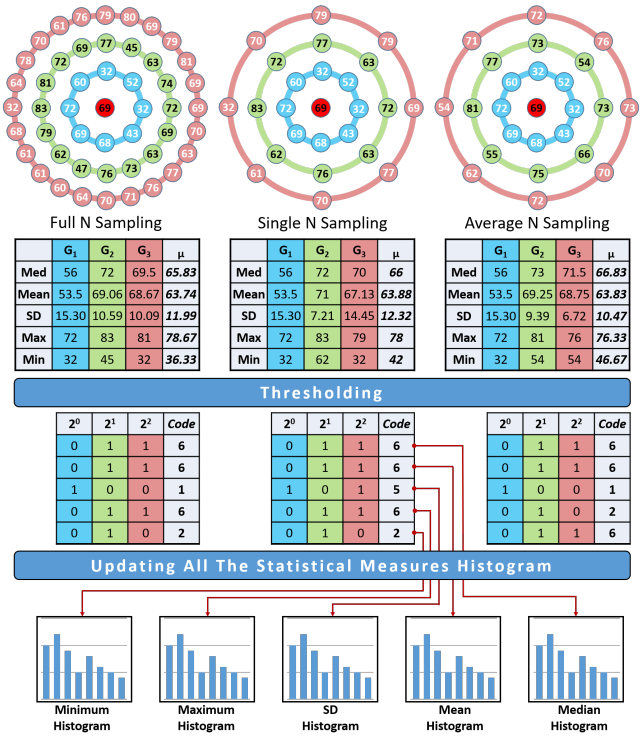

Fig. 2. Illustration of ALBP code calculation

level R increased, more pixels are expected to get involved in the calculation.

There are three sampling methodologies that are used to resample the surrounding pixels, namely; full N, single N, and average N (see Figure 3). The full N resampling is trying to involve all the points on the circle around the center. Of course, it is impossible to add all the points on the circle, as it is an infinite number. The number of points that will be used in each level will increase with respect to the level number. In the full N resampling, the number of points at any level R will be $8 * R$. In other words, every time the level is increased by one, 8 more points are added. The drawback of that technique is the huge amount of computations, specially when the R is large and for there are points that need bilinear interpolation. To overcome this issue, the single N resampling technique could be utilized, as it will only involve a fixed number of pixels (8 pixels on each level regardless of the R).This technique will solve the problem of the computation cost but will lose a lot of data, especially for the large values of R. To overcome this issue and to compromise between the previous two techniques, an average N resampling could be used. Average N resampling uses all the pixels and calculates the average to 8 sets of the pixels. This technique allows us to use the the complete available data and reduce them to the same number of the single N resampling as shown in the following equation:

$$|G_R| = \begin{cases} 8 * R & \text{full N sampling} \\ 8 & \text{single and average N sampling} \end{cases} \quad (4)$$

All these resampling techniques are experimented and compared together to obtain the highest classification accuracy.

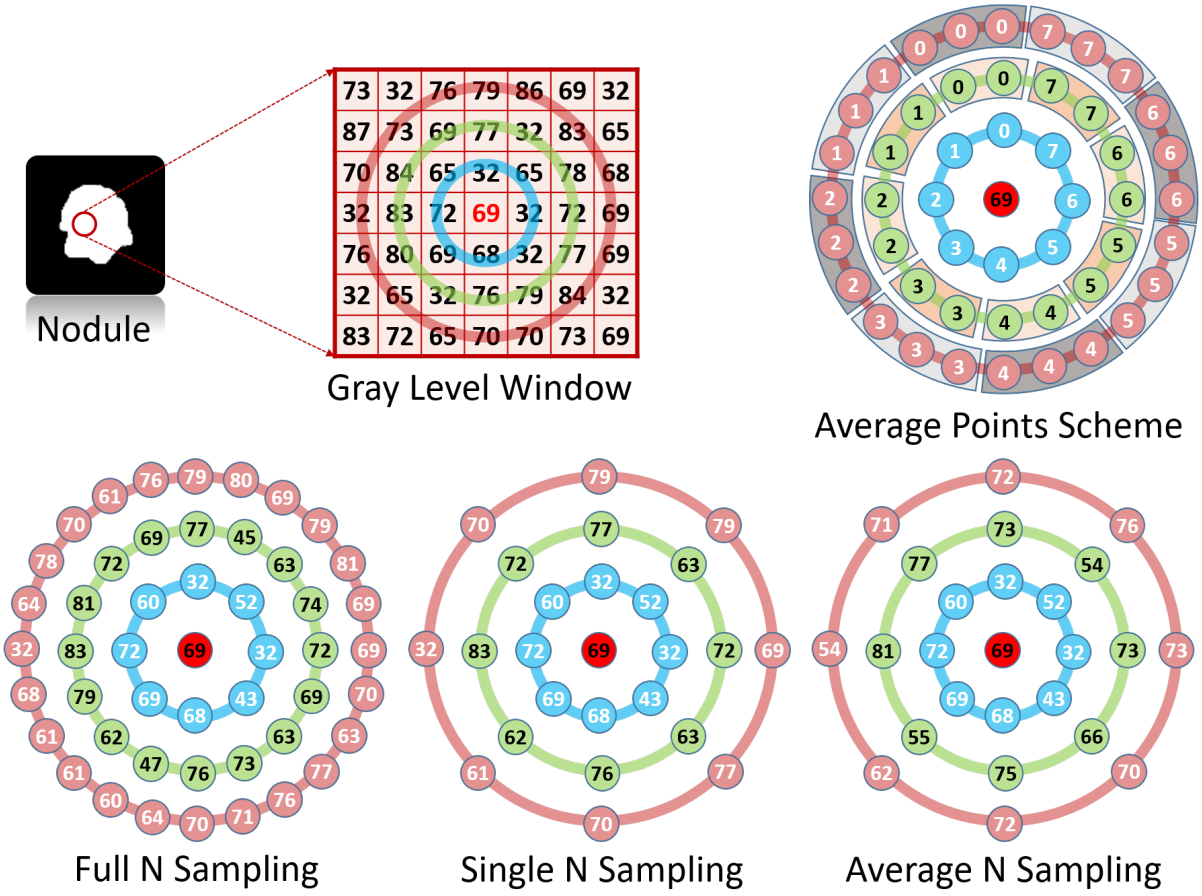

Fig. 3. Different examples for the resampling techniques

(ii) Gray level distribution analysis

Adding more than one level of pixels will increase the dimensionality. So, there is a real need to reduce the dimensionality without losing any texture information. The statistical analysis of the gray level distribution will reduce the dimensionality after taking into account the whole information and present it in a way that makes it easy to analyze. The median value that separates the largest half from the smallest half is one of the used measures. The main disadvantage of that measure is not taking into account the whole data (the median value will remain the same regardless the increase in the highest value or the decrease in the lowest value). So, we need to add more measures like the mean, which indicates the data average and the standard deviation that shows how much the data differs from the average. The maximum and minimum has been also added to the list of the statistical measures that are calculated for the gray level of the neighborhood pixels. Formally, for each level R, it representation could be reduced by the transform: $\phi_R : \mathbb{R}^N \rightarrow \mathbb{R}^5$. All these measures will give summarized information about the gray level distribution that will enable us to distinguish between the homogeneous texture and nonhomogeneous one that characterize the benign and malignant nodules respectively. For every level R a set of the mentioned measures are calculated for G_R. This representation reduces the dimensionality from any domain size to $\mathbb{R}^5$. The expected output from this phase is the vectors $\mathbf{D}_R$ for each level radius R.

(iii) Construction of the feature vector

As mentioned before, the traditional LBP and most of its variations are using the central pixel to threshold the surrounding neighbor pixels. Here, The surrounding pixels gray level are replaced by the distribution analysis measures vector which is calculated from the previous phase. This vector is thresholded using the average of every statistical measure over all the levels. This thresholding vector is denoted by μ and could be calculated using the following equation:

$$\mu = \frac{1}{R} \begin{bmatrix} \sum_{i=1}^{R} Median_i \\ \sum_{i=1}^{R} Mean_i \\ \sum_{i=1}^{R} SD_i \\ \sum_{i=1}^{R} Min_i \\ \sum_{i=1}^{R} Max_i \end{bmatrix} \tag{5}$$

The binary code will be calculated for every statistical measure separately and its histogram will be updated separately. For example, the binary code for the mean could be calculated

using the following equation:

$$ALBP_R = \sum_{i=1}^{R} 2^{i-1} * f(mean(G_i) - \mu(mean)) \quad (6)$$

where:

$$f(x) = \begin{cases} 1 & \text{if } x \geq 0 \\ 0 & otherwise \end{cases} \quad (7)$$

B. Spherical Harmonic

The complexity of the nodule's surface is an important feature that can be used as a discriminatory feature to differentiate between benign and malignant nodules. This complexity stems from the hypothesis that the growth rate of malignant nodules is higher than the benign ones and this leads to such irregularity/complexity in the shape. To capture this characteristic, we used our modeling for the shape complexity description using spherical harmonics (SHs) decomposition of the given nodule and extracting the reconstruction error, (between the original nodule and the constructed one), as the input feature to our framework. In the modeling of the shape complexity using SHs, each nodule surface is modeled as a linear combination of basis functions. First, the surface of the nodule is approximated in a discrete way using triangular 3D mesh. Consequently, that surface is mapped to the unit sphere using our Attraction-Repulsion algorithm [23] to provide accurate modeling by keeping the distance from the nodule's center to each node on the surface equal to one and also maintains an equal distance between each node and all of its neighbors. Following the mapping of the nodule surface to the unit sphere, the nodule is represented as a linear combination of SHs and the order of the harmonics will be used as a representation of the shape complexity. Lower-orders will be enough to represent simple shapes, (benign nodules), while higher-orders will be required to represent more complex shapes, (malignant nodules). The solution of the isotropic heat equation for the nodule surface on the unit sphere is used to estimate the coefficients of the linear combination. These coefficients will be used in the reconstruction process using iterative residual fitting [24].

C. Dimensionality reduction and nodule diagnosis

A stacked autoencoder that consists of three hidden layers is used to reduce the dimensionality of the modeled features. Each hidden layer reduces 30% of the input features. By the third layer, the last feature vector is reduced to almost 34% of the original feature vector size. A softmax classifier is used separately for each descriptor, after each autoencoder network, to provide an initial diagnosis probability for each descriptor. Finally, the output probability of the first stage is combined and fed to another autoencoder and softmax classifier to give us the final estimation of the diagnosis probability of the nodule. The second stage helps assigning different weights to the input descriptors, which will enhance the final diagnosis accuracy.

III. Experimental Results

We used to evaluate our method the publicly available LIDC dataset [25]. The dataset is composed of $1,080$ lung cases where each case is composed of multiple CT scans along with (XML) files that annotate the lung nodules. For almost each case, the annotation is provided by four radiologists where each of them give his unique description of the nodule along with its characteristics. Every nodule description provided by each one of the four radiologists is composed of the ground truth contour of the nodule along the x, y and z direction and a rank of each nodule going from 1 to 5, with a score of 1 for a nodule that is in their opinion most likely to be benign and 5 for a nodule that is most likely to be malignant. As may be concluded, radiologists may disagree on the label of the nodule and its score given the fact that this annotation is only based on looking into the CT scans not on biopsy. This made us turn toward generating our collection based on a majority vote for the four radiologists.

In other words if the average score of the four radiologists for each nodule case is greater than ≥ 3.5 we label the nodule as malignant and if the average score is less than or equal to ≤ 1.5 we consider the nodule to be benign. This way of extracting our used dataset resulted in a total number of 727 nodules, (314 malignant and 413 benign), used for training and testing. Samples have been obtained by applying $3D$ window centric with the nodule center and of size $40 \times 40 \times 40mm^3$

The data was divided into two groups, 70% and 30% for training and testing, respectively. Our framework is evaluated using different accuracy measures such as: accuracy, true positive rate (TPR), true negative rate (TNR) and area under the receiver operating characteristics curve.

Multi-view ALBP has many parameters that require tuning in order to achieve the best accuracy such as the number of levels used around the center point, the used resampling scheme, and the number of views. From figure 4, We could conclude easily that the single N resampling has the lowest accuracy among all the resampling schemes regardless the other parameters. Moreover, the average N and full N has no noticeable difference in the accuracy which make the average N resampling scheme the best when we take into account the calculations cost. Also, The experiments show that the best accuracy was achieved when five views are used for the 3D volume while involving three levels of neighbors around the central pixel.

As mentioned before in the spherical harmonic section, the lung nodule can be reconstructed using different orders of spherical harmonics. When higher orders of the spherical harmonics are used, the reconstruction error will be decreased, but the number of the calculation will be increased. The number of the used orders of spherical harmonics needs to be optimized to be able to describe the nodule shape without doing unneeded calculations. Figure 5 shows the average reconstruction error curve for all the dataset nodules. The average reconstruction error for the nodules after 65 spherical harmonic is less than 0.1, which could be considered as a

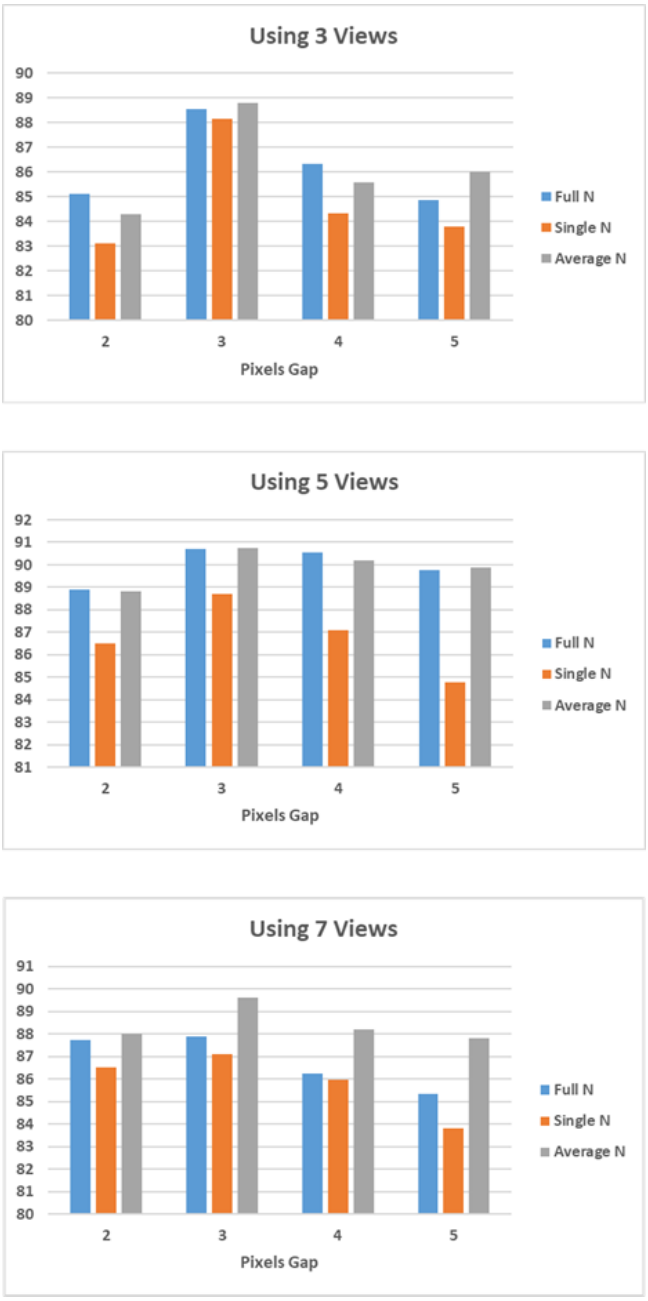

Fig. 4. Multi-view ALBP accuracy using different parameters

negligible error. In our experiment, we used 70 spherical harmonics in order to avoid over fitting to the used dataset.

In order to understand the impact of each feature on the overall accuracy independently, table I report the accuracy measures for each feature separately, as well as the combined framework. Also a comparison with other modern frameworks that uses the LIDC database are included in table I.

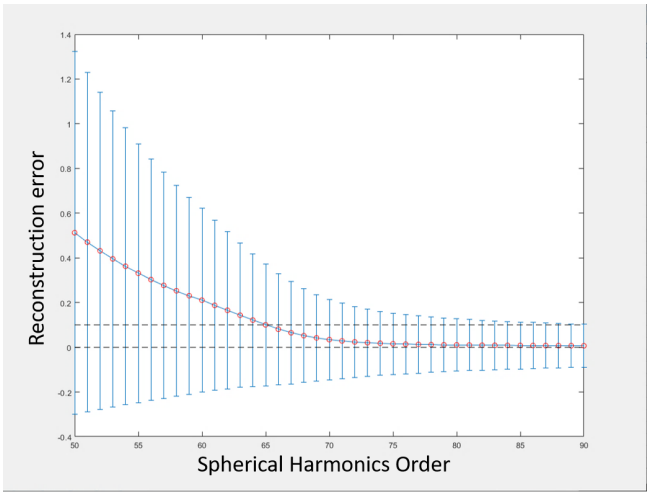

Fig. 5. Average error curves of the nodule reconstruction using different spherical harmonics orders.

TABLE I
CLASSIFICATION RESULTS

	Evaluation Metrics		
	Accuracy	TPR	TNR
Multi-view ALBP	90.73	90.57	92.19
Spherical Harmonics	89.82	93.55	87.20
Combined Features	**93.79**	**94.36**	**92.80**
Ren et al [16]	90.00	81.00	95.00
Al-Shabi et al [26]	92.81	92.36	93.21
Ren et al [16]	90.00	81.00	95.00
Liu et al [13]	92.92	93.84	91.62

IV. CONCLUSION

In conclusion, this manuscript presented a new CAD system for pulmonary nodule diagnosis either malignant or benign by using various handcrafted features. Multi-view ALBP is implemented to characterize the pulmonary nodule texture. Some special functions called spherical harmonics are used to characterize the nodule contour. Finally, all these features are reduced using a stacked autoencoder and classified using a probability-based linear classifier to give the final diagnosis of the nodules.

The feasibility of the presented framework is validated using cases from LIDC database and its effectiveness is confirmed by comparing its result with other state-of-art frameworks. A quantitative comparison with recently developed diagnostic techniques highlights the advantages of the proposed framework over state-of -the-art ones. Moreover, we plan to file an IRB protocol in the future and locally collect data at our site to test on subjects that have malignant/benign nodules with biopsy confirmations.

REFERENCES

[1] American Cancer Society, "Cancer Facts and Figures," 2021.

[2] A. Traverso, "Development and application in clinical practice of computer-aided diagnosis systems for the early detection of lung cancer," 2019.

[3] A. S. Eltrass and M. S. Salama, "Fully automated scheme for computer-aided detection and breast cancer diagnosis using digitised mammograms," *IET Image Processing*, vol. 14, no. 3, pp. 495–505, 2019.

[4] L. B. da Cruz, D. A. D. Júnior, J. O. B. Diniz, A. C. Silva, J. D. S. de Almeida, A. C. de Paiva, and M. Gattass, "Kidney tumor segmentation from computed tomography images using deeplabv3+ 2.5 d model," *Expert Systems with Applications*, vol. 192, p. 116270, 2022.

[5] M. S. Salama, A. S. Eltrass, and H. M. Elkamchouchi, "An improved approach for computer-aided diagnosis of breast cancer in digital mammography," in *2018 IEEE international symposium on medical measurements and applications (MeMeA)*. IEEE, 2018, pp. 1–5.

[6] O. J. Pellicer-Valero, J. L. Marenco Jiménez, V. Gonzalez-Perez, J. L. Casanova Ramón-Borja, I. Martín García, M. Barrios Benito, P. Pelechano Gómez, J. Rubio-Briones, M. J. Rupérez, and J. D. Martín-Guerrero, "Deep learning for fully automatic detection, segmentation, and gleason grade estimation of prostate cancer in multiparametric magnetic resonance images," *Scientific reports*, vol. 12, no. 1, pp. 1–13, 2022.

[7] A. Kalsoom, M. Maqsood, S. Yasmin, M. Bukhari, Z. Shin, and S. Rho, "A computer-aided diagnostic system for liver tumor detection using modified u-net architecture," *The Journal of Supercomputing*, pp. 1–23, 2022.

[8] A. S. Musallam, A. S. Sherif, and M. K. Hussein, "A new convolutional neural network architecture for automatic detection of brain tumors in magnetic resonance imaging images," *IEEE Access*, 2022.

[9] W. Safta and H. Frigui, "Multiple instance learning for benign vs. malignant classification of lung nodules in CT scans," in *2018 IEEE International Symposium on Signal Processing and Information Technology (ISSPIT)*. IEEE, 2018, pp. 490–494.

[10] J. Chen, H. Zeng, C. Zhang, Z. Shi, A. Dekker, L. Wee, and I. Bermejo, "Lung cancer diagnosis using deep attention based on multiple instance learning and radiomics," *arXiv preprint arXiv:2104.14655*, 2021.

[11] W. Safta, M. M. Farhangi, B. Veasey, A. Amini, and H. Frigui, "Multiple instance learning for malignant vs. benign classification of lung nodules in thoracic screening ct data," in *2019 IEEE 16th International Symposium on Biomedical Imaging (ISBI 2019)*. IEEE, 2019, pp. 1220–1224.

[12] E. S. Neal Joshua, D. Bhattacharyya, M. Chakkravarthy, and Y.-C. Byun, "3d cnn with visual insights for early detection of lung cancer using gradient-weighted class activation," *Journal of Healthcare Engineering*, vol. 2021, 2021.

[13] D. Liu, F. Liu, Y. Tie, L. Qi, and F. Wang, "Res-trans networks for lung nodule classification," *International Journal of Computer Assisted Radiology and Surgery*, pp. 1–10, 2022.

[14] C.-J. Lin, S.-Y. Jeng, and M.-K. Chen, "Using 2d cnn with taguchi parametric optimization for lung cancer recognition from ct images," *Applied Sciences*, vol. 10, no. 7, p. 2591, 2020.

[15] N. Kalaivani, N. Manimaran, S. Sophia, and D. Devi, "Deep learning based lung cancer detection and classification," in *IOP Conference Series: Materials Science and Engineering*, vol. 994, no. 1. IOP Publishing, 2020, p. 012026.

[16] Y. Ren, M.-Y. Tsai, L. Chen, J. Wang, S. Li, Y. Liu, X. Jia, and C. Shen, "A manifold learning regularization approach to enhance 3d ct image-based lung nodule classification," *International Journal of Computer Assisted Radiology and Surgery*, vol. 15, no. 2, pp. 287–295, 2020.

[17] S. Suresh and S. Mohan, "Roi-based feature learning for efficient true positive prediction using convolutional neural network for lung cancer diagnosis," *Neural Computing and Applications*, pp. 1–21, 2020.

[18] H. Jiang, F. Gao, X. Xu, F. Huang, and S. Zhu, "Attentive and ensemble 3d dual path networks for pulmonary nodules classification," *Neurocomputing*, vol. 398, pp. 422–430, 2020.

[19] S. B. Shrey, L. Hakim, M. Kavitha, H. W. Kim, and T. Kurita, "Transfer learning by cascaded network to identify and classify lung nodules for cancer detection," in *International Workshop on Frontiers of Computer Vision*. Springer, 2020, pp. 262–273.

[20] V. Patel, S. Shah, H. Trivedi, and U. Naik, "An analysis of lung tumor classification using svm and ann with glcm features," in *Proceedings of First International Conference on Computing, Communications, and Cyber-Security (IC4S 2019)*. Springer, 2020, pp. 273–284.

[21] T. Ojala, M. Pietikainen, and T. Maenpaa, "Multiresolution gray-scale and rotation invariant texture classification with local binary patterns," *IEEE Transactions on pattern analysis and machine intelligence*, vol. 24, no. 7, pp. 971–987, 2002.

[22] T. Ojala, M. Pietikainen, and D. Harwood, "Performance evaluation of texture measures with classification based on kullback discrimination of distributions," in *Proceedings of 12th international conference on pattern recognition*, vol. 1. IEEE, 1994, pp. 582–585.

[23] A. Shaffie, A. Soliman, M. Ghazal, F. Taher, N. Dunlap, B. Wang, A. Elmaghraby, G. Gimel'farb, and A. El-Baz, "A new framework for incorporating appearance and shape features of lung nodules for precise diagnosis of lung cancer," in *2017 IEEE International Conference on Image Processing (ICIP)*. IEEE, 2017, pp. 1372–1376.

[24] M. K. Chung, K. M. Dalton, L. Shen, A. C. Evans, and R. J. Davidson, "Weighted fourier series representation and its application to quantifying the amount of gray matter," *IEEE transactions on medical imaging*, vol. 26, no. 4, pp. 566–581, 2007.

[25] S. G. Armato III, G. McLennan, L. Bidaut, M. F. McNitt-Gray, C. R. Meyer, A. P. Reeves, B. Zhao, D. R. Aberle, C. I. Henschke, E. A. Hoffman *et al.*, "The lung image database consortium (LIDC) and image database resource initiative (IDRI): a completed reference database of lung nodules on CT scans," *Medical physics*, vol. 38, no. 2, pp. 915–931, 2011.

[26] M. Al-Shabi, K. Shak, and M. Tan, "3d axial-attention for lung nodule classification," *International journal of computer assisted radiology and surgery*, vol. 16, no. 8, pp. 1319–1324, 2021.